Control of the Folding Dynamics of Self-Reconfiguring Magnetic Microbots Using Liquid Crystallinity

C. Wyatt Shields IV[1,2†], Young-Ki Kim[3,4†], Koohee Han[1,5], Andrew C. Murphy[1], Alexander J. Scott[1], Nicholas L. Abbott[3]* & Orlin D. Velev[1]*

[†]*Authors contributed equally*

[1] Department of Chemical & Biomolecular Engineering, North Carolina State University, Raleigh, NC 27695, USA

[2] Department of Chemical & Biological Engineering, University of Colorado, Boulder, 3415 Colorado Avenue, Boulder, CO 80303, USA

[3] Robert Frederick Smith School of Chemical and Biomolecular Engineering, Cornell University, Ithaca, NY 14853, USA

[4] Department of Chemical Engineering, Pohang University of Science and Technology, 77 Cheongam-Ro, Nam-Gu, Pohang, Gyengbuk 37673, Korea

[5] Materials Science Division, Argonne National Laboratory, Lemont, IL 60439, USA

**** Corresponding authors:*** *odvelev@ncsu.edu and nabbott@cornell.edu*

Keywords: Active Particles, Reconfigurable Assemblies, Liquid Crystals, Microbots, Micromachines

Abstract

Reconfigurable microdevices are being explored in a range of contexts where their life-like abilities to move and change shape are important. While much work has been done to control the motion of these microdevices by engineering their geometry and composition, little is known about their dynamics in complex fluid environments with non-Newtonian rheology. Here, we show how the actuation dynamics of reconfigurable microdevices made by assembly of patchy magnetic microcubes, which we refer to as “microbots”, can be modulated by their interactions with the anisotropic viscoelastic environment of a liquid crystal (LC). We show that the free energy arising from the elastic strain of LC and formation of topological defects around the microbots influences their folding dynamics, which can be tuned by tailoring both the far-field orientation of the LC and the local ordering of the LC at the microbot surfaces. These findings represent a first step towards establishing a general set of design rules to control the dynamics of microbots using complex anisotropic fluids.

Short Summary and Table of Contents Figure

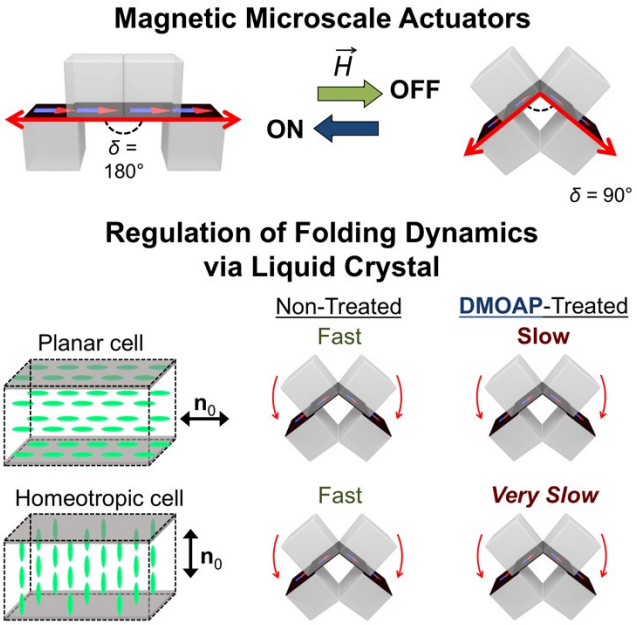

In article number XXXXXXX, Orlin Velev, Nicholas Abbott and co-workers describe how the folding dynamics of microactuators can be regulated in liquid crystal medium. Free energy arising from the elastic strain of liquid crystal and topological defects formed around the actuators can be tuned by surface modifications to program microbot folding dynamics in complex fluids, including foams, gels, blood, and mucus.

1. Introduction

Reconfigurable microdevices have become a subject of intense research interest due to their ability to harvest energy and change shape on demand.[1-3] These attributes allow them to be used as microrobotic structures,[4-5] constituents of self-healing materials,[6-7] and switchable metamaterials.[8-9] Yet, progress in this field is limited by inadequate control over microstructure dynamics in complex fluid media, which has hindered their implementation into practical systems. Earlier work has been done to engineer the shape, composition, and means of energization of reconfigurable microdevices.[10-15] These studies have investigated the acoustic, magnetic, electric, or catalytic manipulation of spheres, ellipsoids, Janus particles, 3D-printed components, and microscale diodes. However, little is known about regulating their dynamics in — and by — complex fluid milieu such as foams, gels, media, blood, and mucus.[16-17]

Here, we show how complex anisotropic fluid media can regulate the dynamics of reconfigurable microdevices in a controlled manner. We used a nematic liquid crystal (LC; 4-pentyl-4-biphenylcarbonitrile (5CB)) as a model complex fluid. Within the LC, molecules exhibit long-range orientational order, indicated by the director **n** (**Figure 1**), leading to anisotropic elasticity and viscosity.[18-19] We investigated how these LC control the dynamics of an emergent class of reconfigurable materials that we refer to as "microbots", which are formed by the directed assembly of patchy magnetic microcubes (Figure 1a).[20] When individually dispersed patchy microcubes are exposed to a uniform magnetic field ($\vec{H}$ = 70 G) in the plane of an optical cell that contains them, the cobalt films (black surface in Figure 1a) along one side of each microcube attain a permanent magnetic dipole that guides their assembly into chains with an angle δ between their dipoles (arms) of 180° (red arrows in Figure 1b). When $\vec{H}$ is removed, the chains of magnetically interacting dipoles release energy through microscale reconfiguration (δ = 90°), while maintaining

the relative sequence of the microcubes due to the residual magnetization of the magnetic films on each particle, thus forming reversibly folding microbots (Figure 1c). These structures can be formed by assembly of as few as three, or as many as tens of cubes. They can be remotely steered using gradient magnetic fields to capture and transport microscale objects such as living cells.[20] In this study, we report how the reconfiguration of these unique structures is mediated by LCs on the microscale, focusing on the example of microbots with an "ABBA" orientational sequence (as defined in Figure 1b; Video 1, Supporting Information).

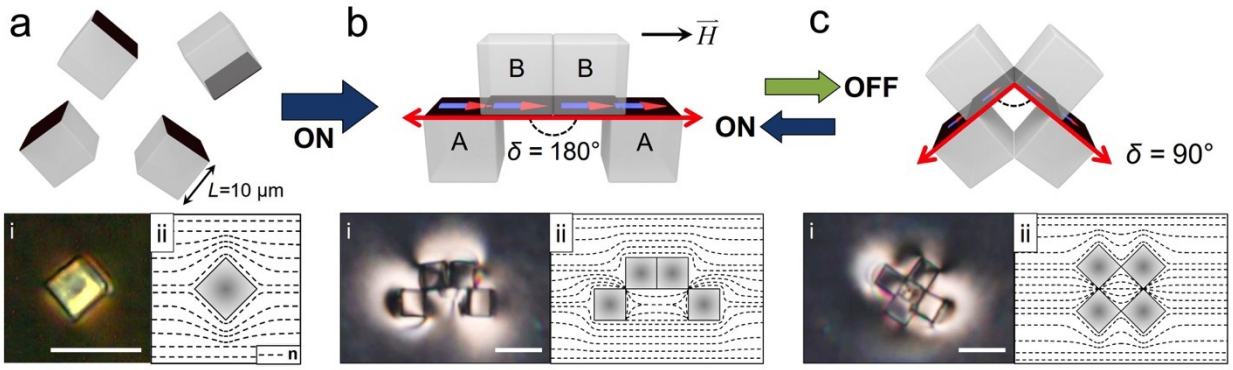

Figure 1. Reconfigurable microbots in liquid crystal (LC). a-c) [Top] Schematic illustrations depicting the magnetic assembly of individual microcubes (a) with edge lengths *L* of 10 μm and cobalt films (black surface) into a microbot with an "ABBA" sequence (b, the angle *δ* between the arms of microbot is 180° under $\vec{H}$ = 70 G), and folding behavior of the microbot upon the removal of the magnetic field (c, *δ* = 90°). Red arrows indicate the arms of the microbot. [Bottom] Corresponding (i) optical micrographs (between crossed polarizers) of microcubes and microbots in a nematic LC (5CB), and (ii) profiles of the director, **n** (dashed lines). Scale bars, 20 μm. Video illustrating the b(i) to c(i) transition is available in the Supporting Information (Video 1).

2. Results and Discussion

2.1 Surface-Dependent Dynamics of Microbots in LC

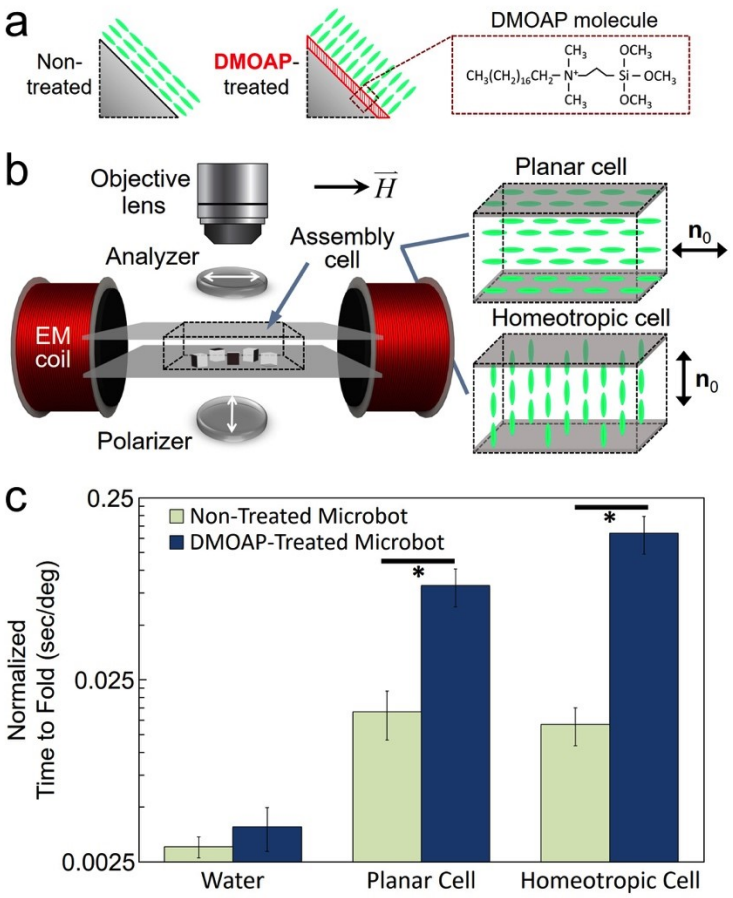

Figure 2. Surface-dependent folding dynamics of microbots in LC. a) Schematic illustrations of the orientation of LCs (green ellipsoids) on microcube surfaces without and with DMOAP treatment. b) Schematic illustration of the experimental setup, comprising a collinear pair of electromagnetic coils and an optical cell (imposing a planar or homeotropic far-field orientation of the LC ($\mathbf{n}_0$)), filled with LC containing microcubes. c) Normalized time for folding of non-treated and DMOAP-treated microbots in water, planar optical cells (optical cells with a planar alignment of $\mathbf{n}_0$), and homeotropic optical cells (optical cells with a vertical alignment of $\mathbf{n}_0$). Video tracking analysis was performed to measure the rate of microbot folding; the normalized time to fold was determined by inverting the rate of folding (1/(degree/sec)). Data represent mean ± standard deviation (S.D.); $N = 4$. Statistical analyses were performed between groups using Tukey's tests; results marked with an asterisk (*) indicate statistical significance ($p < 0.05$).

We report the reconfiguration of microbots presenting two types of surfaces to the LC environment (**Figure 2**a): (i) non-treated surfaces (i.e., native photoresist (SU-8) and cobalt) and

(ii) surfaces treated with dimethyloctadecyl [3-(trimethoxysilyl) propyl] (DMOAP). The optical cells within which the LC resided were assembled from two glass plates with a fixed gap of 100–300 μm. To prepare the optical cell with a planar alignment of $\mathbf{n}_0$ (planar optical cell; Figure 2b), the glass substrates were spin-coated with polyimide PI2555 and rubbed unidirectionally. For the optical cell with a homeotropic alignment of $\mathbf{n}_0$ (homeotropic optical cell; Figure 2b), the glass substrates were spin-coated with polyimide SE5661.

We found that **n** of the 5CB aligned parallel (planar anchoring) and perpendicular (homeotropic anchoring) to the surfaces of microcubes without and with DMOAP treatment, respectively (Figure 2a); justification for these statements is provided below in the context of **Figure 3**. We measured the average time for each microbot to self-fold from an outstretched configuration ($\delta = 180°$; Figure 1b) to a folded configuration ($\delta \approx 90°$; Figure 1c) between crossed polarizers (Figure 2b). Interestingly, the folding dynamics of microbots in LC were strongly influenced by surface properties of the microbots (Figure 2a) and the optical cells that contained them (Figure 2b), while their dynamics were similar in water, an isotropic liquid (Figure 2c). Specifically, in both planar and homeotropic optical cells, the folding of DMOAP-treated microbots took a longer time than that of non-treated microbots (Figure 2c). Furthermore, DMOAP-treated microbots displayed longer folding times in homeotropic optical cells than in planar optical cells, whereas non-treated microbots exhibited similar dynamics in both optical cells. Together, these results suggest that the surface-induced ordering of LCs (both on the microbots and on the confining surfaces of the optical cells) plays a critical role in determining the folding dynamics of the microbots.

We hypothesized that the disparity in the folding times of microbots (Figure 2c) is a result of changes in the LC free energy arising from elastic strain and topological defects (regions where

n is discontinuous), both of which are dependent on surface-induced ordering of LCs. When microscale inclusions are introduced into a nematic host, the director **n** around the inclusions is determined by the elastic strain energy of the LC ($K r_I$) and the surface anchoring energy ($W r_I^2$) associated with preferential orientation of **n** at the inclusion surface, where K is the Frank elastic constant of the LC, W is the surface anchoring energy density, and r_I is the radius (size) of the microinclusion.[21-25] For typical thermotropic nematic LCs such as 5CB, $K \sim 10^{-12}$ N and $W \sim 10^{-5} - 10^{-6}$ J/m^2.[24] As our microcubes have edge lengths (L) of 10 μm, which is larger than K/W = 0.1 – 1.0 μm (i.e., $W r_I^2 > K r_I$), the microcubes reorient the neighboring LCs from $\mathbf{n}_0$. The microcubes thus generate distinct sets of topological defects to satisfy the topological conservation law (theorems of Poincaré and Gauss) that demand a certain number of singularities around microinclusions with a non-zero Euler characteristic (e.g., 1 for a square, 2 for a cube).[24-32]

2.2 Local Orientation of LC Around Microcubes

To test our hypothesis that the free energies of the LC elastic strain and topological defects modulate the folding dynamics of the microbots, we first determined the preferential orientation of **n** at the microbot surfaces without and with DMOAP treatment. To this end, we examined single microcubes dispersed in 5CB LC in planar optical cells between crossed-polarizers (Figure 3) and made three key observations. First, as previously reported for cuboidal inclusions dispersed in LC,[33-36] we found that microcubes without and with DMOAP treatment diagonally aligned their bodies to $\mathbf{n}_0$ and exhibited birefringent edges (Figure 3a,e), indicating that the near-surface **n** deviates from $\mathbf{n}_0$ (and thus from the optical axes of the polarizers). Second, when viewed with a retardation plate of wavelength λ = 530 nm with its slow axis (**s**) at 45° to the polarizers, a higher order interference color (blue; Figure 3b) was observed at the surfaces of native microcubes

parallel to **s**, suggesting a planar alignment of **n** at the surface of the microbots (see inset in Figure 3b).[37-39] Conversely, the surfaces of DMOAP-treated microcubes exhibited a lower order interference color (yellow; Figure 3f), suggesting a homeotropic alignment of **n** at the microbot surface. Third, we found defects at corners of the native microcube (indicated by circles in Figure 3c), but a Saturn-ring defect around DMOAP-treated microcubes (indicated by an ellipsoid in Figure 3g). This LC organization is consistent with planar anchoring on non-treated surfaces and homeotropic anchoring on DMOAP-treated surfaces (Figure 2a).[40-42] Together, the above observations reveal that the surfaces of non-treated microcubes (both SU-8 and cobalt) impose planar anchoring of the LC, but DMOAP treatment provides a direct means by which the preferential orientation of LCs on the microcube surfaces are switched to a homeotropic anchoring. The inferred surface alignments of **n** were confirmed by independent optical investigations on LCs supported on SU-8 coated substrates (Figure S1, Supporting Information). We note here that the DMOAP treatment of silica and chromium were reported earlier to impose a homeotropic alignment,[40-44] but DMOAP-treated SU-8 surfaces have not, to our knowledge, been previously reported.

From the optical characterization discussed above and by assuming that the microcubes exhibit strong surface anchoring (i.e., near-surface **n** is strictly tangential or homeotropic), we mapped the director fields and associated sets of topological defects around the microcubes (Figure 3d,h). To satisfy the conservation law,[24-32] the defects observed at the corners of non-treated microcubes (circles in Figure 3c) should correspond to line defects (disclinations) along edges perpendicular to $\mathbf{n}_0$ (// z; axes defined in Figure 3a) with topological strengths of $m = +1/4$ (red dots in Figure 3d) and $m = -1/2$ (blue dots in Figure 3d). In contrast, the DMOAP-treated microcubes exhibited a disclination loop of $m = -1/2$ (Saturn-ring defect; ellipsoid in Figure 3g

and blue lines and dots in Figure 3h), and thus must possess surface disclinations of m = +1/4 at all edges (red dots and lines in Figure 3h).

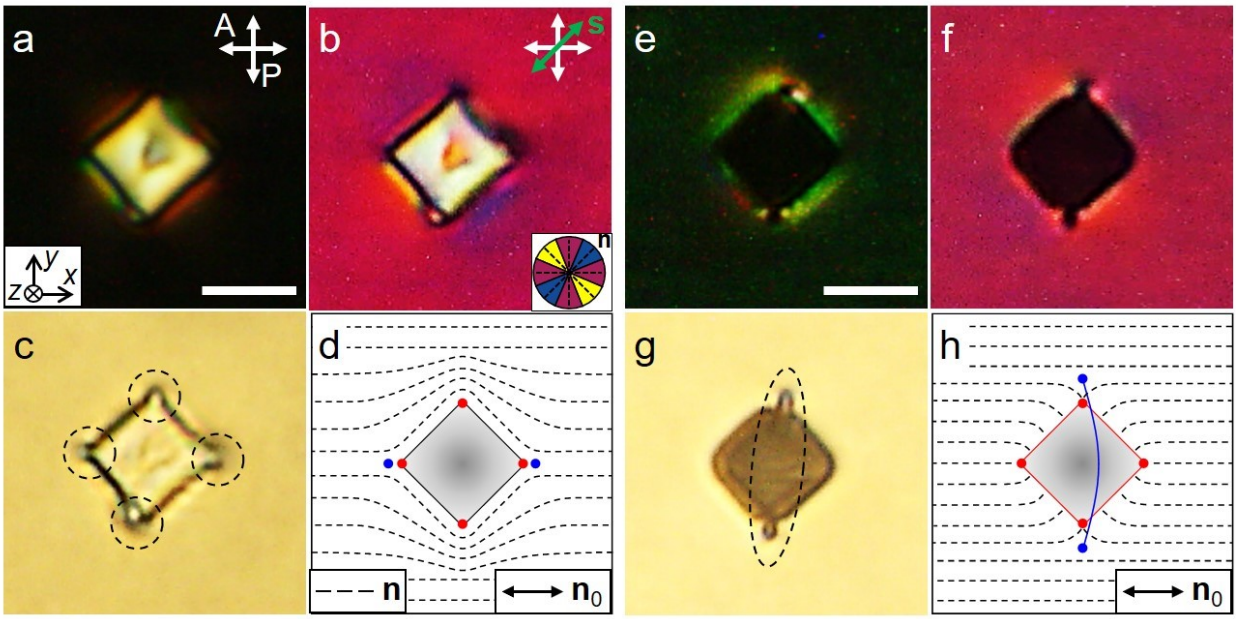

Figure 3. Elastic strain and topological defects around microcubes in planar optical cells. Micrographs (a-c and e-g) and corresponding maps (d,h) of director fields and topological defects for a microcube without (a-d) and with DMOAP surface treatment (e-h) in planar optical cells. Scale bars, 10 μm. P, A, **s**, and $\mathbf{n}_0$, respectively, indicate the polarizations of a polarizer and analyzer, the slow axis of a retardation plate of wavelength λ = 530 nm, and the far-field orientation of LCs. Inset in (b) indicates the orientation-dependent interference colors of LC between crossed polarizers with the retardation plate. In (d,h), red dots indicate surface line defects (disclinations) of m = +1/4 at the edges of the microcube along the z-axis (circles in c), red lines indicate surface disclinations of m = +1/4 at the edges of the microcube in x-y plane, and blue lines and dots indicate disclinations of m = –1/2 around the microcube (circles in c,g).

2.3 Elastic Strain and Topological Defects Around Microbots in Planar Optical Cells

Having determined the orientation of the LC at the surfaces of individual microcubes, we mapped the LC director and associated topological defects around assembled microbots with and without $\vec{H}$ and compared the LC elastic and defect energies in planar optical cells ($\mathbf{n}_0$ // x; **Figure 4** and

Figure S2, Supporting Information). In the presence of $\vec{H}$ (// x), the non-treated microbots exhibited six point defects of $m = -1/2$ at the center of their surfaces (circles in Figure 4a(i) and open blue dots in Figure 4a(iii)). To satisfy the conservation law,[24-32] we predicted that surface disclinations of $m = +1/4$ form along the edges of microbot surfaces in the y-z plane (red dots and lines in Figure 4a(iii)), although it is difficult to experimentally locate surface disclinations.[34] When $\vec{H}$ was removed, however, the non-treated microbots folded and no longer possessed the point defects, leading to the formation of disclinations of $m = +1/4$ and $-1/2$ (red and blue dots in Figure 4b(iii), respectively) along the edges perpendicular to $\mathbf{n}_0$. The difference in the LC elastic and defect energies (ΔE_1) of the two states of a microbot in a planar optical cell can be evaluated by expressions detailed earlier and adapted here:[18, 25, 45-47]

$$\Delta E_1 = E_1^{\text{off}} - E_1^{\text{on}} = \left[-A\pi KL + 8\pi K(r_c - S) + \frac{1}{2}\pi KL \ln\left(\frac{4S^3}{r_c^3}\right)\right]_{\text{elastic}} + \left[\frac{1}{2}\pi r_c{}^2(3L - 8r_c)\varepsilon_c\right]_{\text{defect}} \quad (1)$$

where A is a numerical constant, S is the characteristic length of the elastic deformation, r_c is the radius of the defect core, and ε_c is the energy density of the defect core (see Supporting Information for details). ΔE_1 calculated from Eq. (1) was found to be -4.67×10^{-16} J ($\approx -11.3\times10^4\ K_B T$ at T = 298 K, where K_B is the Boltzmann constant and T is the temperature), indicating that the off-state (folded; Figure 4b) is energetically favored by the LC. We note that the elastic energy (E_e, first term in ΔE_1) is larger than the defect energy (E_d, second term in ΔE_1); $E_e/E_d = -2.7$ in ΔE_1. Furthermore, E_d is positive, indicating that the defect-related contribution to the LC free energy opposes the folding process. This can be understood by comparison of Figure 4a(iii) and Figure 4b(iii); the folding process increases the number of microcube vertices in contact with LC and thus the number of LC defects.

Next, we considered the LC-mediated dynamics of microbots with DMOAP-treated surfaces in planar optical cells. Due to strong surface anchoring, the DMOAP-treated microbots formed surface disclinations of $m = +1/4$ at all edges contacting 5CB (red dots and lines in Figure 4c(iii), d(iii)); the total length of the disclinations is 40 L in the outstretched configuration (Figure 4c(iii)) and 48 L in the folded configuration (Figure 4d(iii)). This expectation is consistent with the observation of three disclination loops of $m = -1/2$ under $\vec{H}$ (ellipsoids in Figure 4c(ii) and blue lines and dots in Figure 4c(iii)) and the appearance of an additional point defect of $m = -1$ upon removal of $\vec{H}$ (black circle in Figure 4d(ii) and black dot in Figure 4d(iii)). The corresponding ΔE_2 is given by:

$$\Delta E_2 = E_2^{\text{off}} - E_2^{\text{on}} = \left[-A\pi KL + \frac{8}{3}\pi K(S - r_c) + \frac{1}{2}\pi KL \ln\left(\frac{4S}{r_c}\right)\right]_{\text{elastic}} + \left[\frac{1}{6}\pi {r_c}^2(3L + 8r_c)\varepsilon_c\right]_{\text{defect}} \quad (2)$$

and was evaluated to be 1.82×10^{-16} J ($\approx 4.4\times10^4$ $K_B T$ at $T = 298$ K); $E_e/E_d = 0.9$ in ΔE_2. The positive value of ΔE_2 found in the microbot with DMOAP-treated surfaces indicates that the folded configuration (off-state; Figure 4d) causes both the LC elastic and defect energy to be greater than the outstretched configuration (on-state; Figure 4c). Thus, upon removal of $\vec{H}$, the elasticity of the LC and defects resist the transition from outstretched-to-folded states for DMOAP-treated microbots ($\Delta E_2 > 0$; Figure 4c,d), whereas they assist the transition of microbots with non-treated surfaces ($\Delta E_1 < 0$; Figure 4a,b). This is consistent with our experimental observations, which reveal a slower folding time of DMOAP-treated microbots as compared to microbots with non-treated surfaces (Figure 2c).

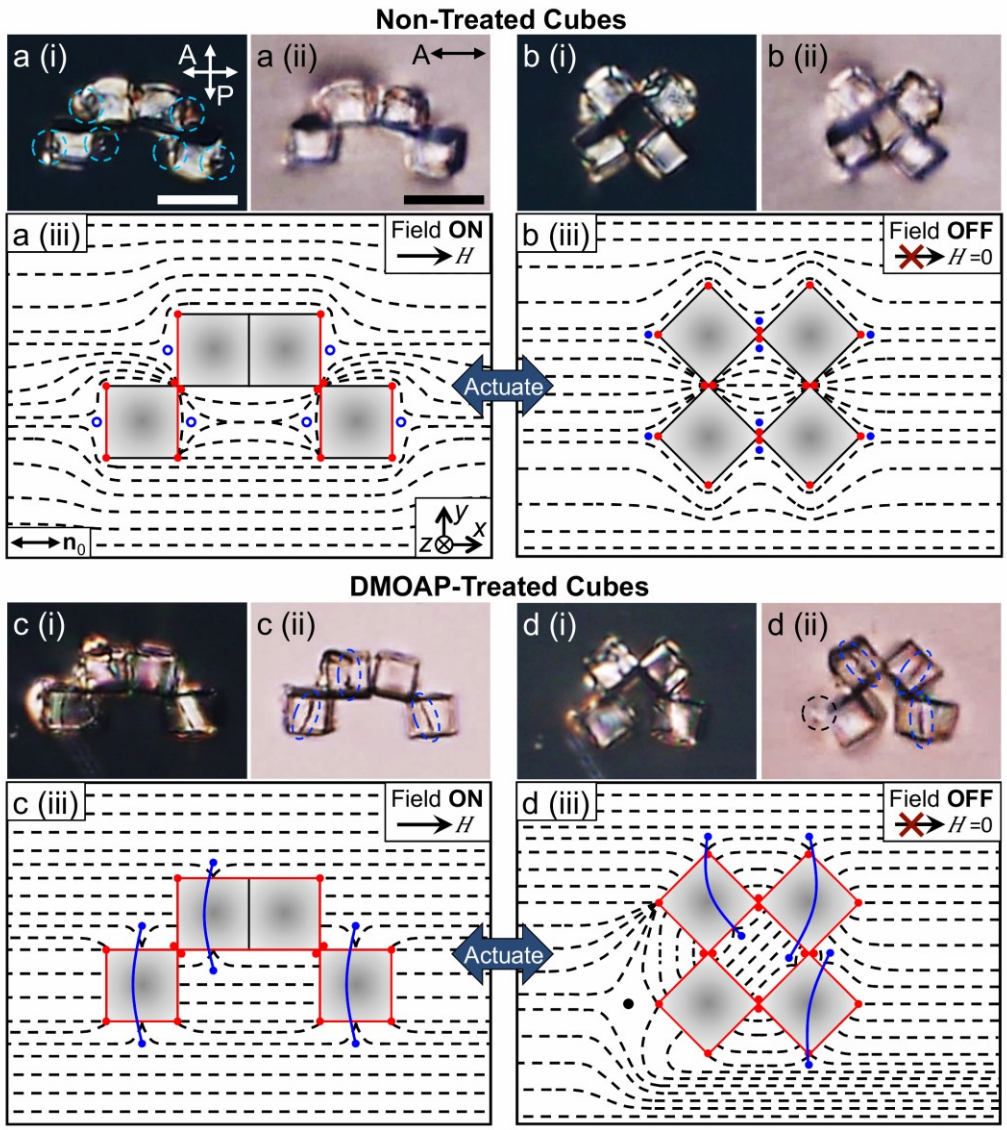

Figure 4. Elastic strain and topological defects around microbots in planar optical cells. a-d) Micrographs (i and ii) and reconstructed maps of director fields and defects (iii) for non-treated (a,b) and DMOAP-treated microbots (c,d) in planar optical cells with (a,c) and without $\vec{H}$ (// $\mathbf{n}_0$ // x; (b,d)). Scale bars, 20 μm. In (iii), open blue dots indicate point defects of m = –1/2 (blue circles in a(i)), solid blue lines and dots indicate disclinations of m = –1/2 (blue ellipsoids in c(ii),d(ii)), red lines (in x-y plane) and dots (along the z-axis) indicate surface disclinations of m = +1/4, and the solid black dot indicates a point defect of m = –1 (black circle in d(ii)). See Figure S2 (Supporting Information) for full configurations of topological defects.

2.4 Elastic Strains and Topological Defects Around Microbots in Homeotropic Optical Cells

We mapped the LC director and topological defects around microbots with and without $\vec{H}$ in homeotropic optical cells ($\mathbf{n}_0$ // z) and determined their elastic-defect energies (**Figure 5**). As illustrated in Figure 5a(iii), b(iii), the microbots yielded the same set of defects (point defects of m = –1/2 (open blue dots), surface disclinations of m = +1/4 (red lines and dots), and disclination loops of m = –1/2 (blue lines)) as those in planar optical cells under $\vec{H}$ (// x; Figure 4a,c and Figure S2, Supporting Information). The differences between the two types of optical cells were that, in homeotropic optical cells, the point defects (open blue dots in Figure 5a(iii)) and surface disclinations (red lines in Figure 5a(iii)) from non-treated microbots and the disclination loops surrounding DMOAP-treated microbots (blue line in Figure 5b(iii)) were generated in the x-y plane, while they formed in the y-z plane of planar optical cells (Figure 4a,c). In the absence of $\vec{H}$, non-treated microbots (Figure 5c) had both surface disclinations of m = +1/4 (red lines in Figure 5c(iii)) and point defects of m = –1/2 (open blue dots in Figure 5c(iii)) in the x-y plane of homeotropic optical cells in contrast to non-treated microbots in planar optical cells that only possessed disclinations of m = +1/4 (red dots in Figure 4b(iii)) and –1/2 (blue dots in Figure 4b(iii)) along the z-axis. For DMOAP-treated microbots, the isolated point defect (black dot in Figure 4d(iii)) no longer persisted and all of the microcubes within the microbot assembly were surrounded by disclination loops of m = –1/2 (blue lines in Figure 5d(iii)) in the x-y plane, which only formed around three microcubes in the planar case (blue lines in Figure 4d(iii)).

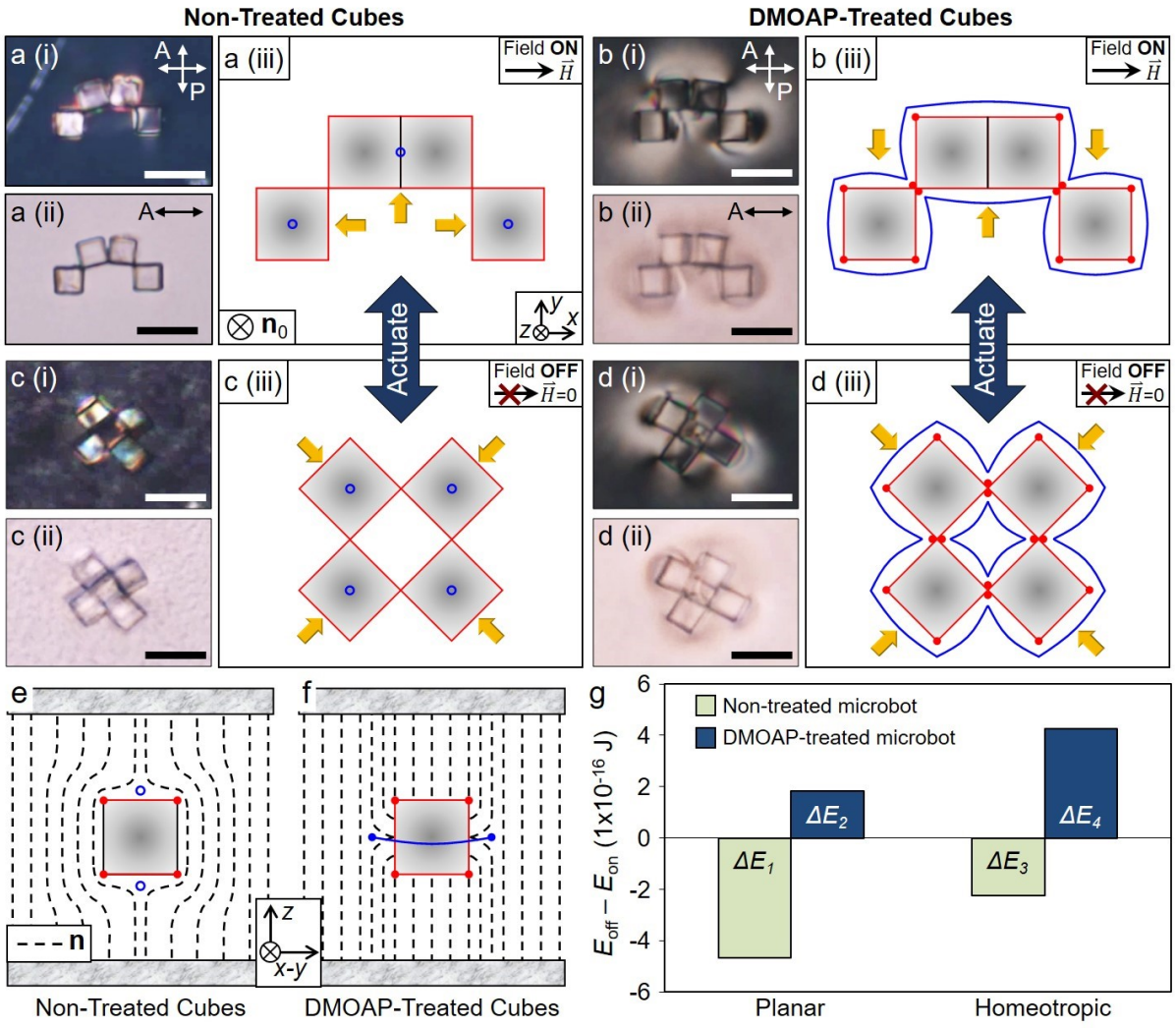

Figure 5. Elastic strain and topological defects around microbots in homeotropic optical cells. a-d) Micrographs (i and ii) and schematic illustrations of defect configurations (iii) for non-treated (a,c) and DMOAP-treated microbots (b,d) in homeotropic optical cells ($\mathbf{n}_0$ // z) with (a,b) and without $\vec{H}$ (// x; c,d). Scale bars, 20 μm. e,f) Director profiles from the view of the yellow arrows in (iii), which correspond to microcubes without (e) and with DMOAP treatment (f). Open blue dots indicate point defects of m = –1/2, blue lines indicate disclination loops of m = –1/2, and red lines and dots indicate surface disclinations of m = +1/4 along the edges of the microcubes. See Figure S2 (Supporting Information) for full configurations of topological defects. g) Differences in the elastic-defect energies between microbots in the off-state (E_{off}, folded) and on-state (E_{on}, outstretched) in planar (Figure 4) and homeotropic (Figure 5a-d) optical cells.

We evaluated the difference in the LC elastic and defect energy for non-treated (ΔE_3) and DMOAP-treated (ΔE_4) microbots in homeotropic optical cells as:

$$\Delta E_3 = E_3^{\text{off}} - E_3^{\text{on}} = \left[-A\pi KL + \frac{8}{3}\pi K(S - r_c) + \frac{1}{4}\pi KL \ln\left(\frac{4S}{r_c}\right)\right]_{\text{elastic}} + \left[\frac{1}{12}\pi {r_c}^2(3L + 16r_c)\varepsilon_c\right]_{\text{defect}} \quad (3)$$

$$\Delta E_4 = E_4^{\text{off}} - E_4^{\text{on}} = \left[-A\pi KL + \frac{1}{2}\pi KL \ln\left(\frac{8S^2}{r_c^2}\right)\right]_{\text{elastic}} + [\pi {r_c}^2 L\varepsilon_c]_{\text{defect}} \quad (4)$$

We determined ΔE_3 to be -2.24×10^{-16} J ($\approx -5.4\times10^4\ K_B T$ at $T = 298$ K) and ΔE_4 to be 4.25×10^{-16} J ($\approx 10.3\times10^4\ K_B T$ at $T = 298$ K), suggesting that in homeotropic cells, the net effect of elastic strain and defects assist the folding actuation of non-treated microbots, yet oppose the actuation of DMOAP-treated microbots; $E_e/E_d = -5.7$ in ΔE_3 and 1.3 in ΔE_4, with $E_d > 0$ in both cases. As $\Delta E_4 > \Delta E_3$, the folding of microbots with DMOAP treatment is expected to be slower, which is in agreement with our experimental observations (Figure 2c).

To summarize our findings with the LC elastic and defect energy, Figure 5g shows the values of ΔE for non-treated and DMOAP-treated microbots in planar and homeotropic optical cells, as calculated from Equations 1-4. These results provide general support our hypothesis that the folding dynamics of microbots (described by their relative folding times; Figure 2c) are correlated with the elastic strain of LCs and topological defects that can be controlled by the surface modification of microbots and boundary surfaces of the optical cells. Thus, our results suggest that modulating the LC elastic and defect energy (and other complex, anisotropic liquids) around microscale actuators provides a new pathway to regulate their folding dynamics. However, we note that the differences in the elastic strain energy are insufficient to fully describe the microbot dynamics, as we observe positive values for the DMOAP-treated microbots. Thus, to analytically resolve the net forces that give rise to the microbot dynamics, we determined the magnetic dipolar force, as described below.

2.5 Overall driving force acting on microbots in LCs

The net force driving the microbot motions arises from the additive contribution of the LC elastic and defect-related forces and the magnetic dipolar force (**Figure 6**). The magnitude of the force arising from the LC elastic and defect energies was estimated by normalizing $\Delta E_{1\text{-}4}$ (Figure 5g) by the net displacement of the microbot arms during folding ($D \approx 16$ μm; Figure 6c (left)). We estimated the magnetic dipolar force by quantifying the opposing viscous drag, which was achieved by measuring the folding speed of microbots in isotropic solutions of known viscosity. Since the microbots were energized by the same field strength in each experiment (i.e., $\vec{H} = 70$ G), we assumed that the magnitude of the magnetic dipolar force was the same in all experiments.[48] Specifically, by using the microbot as "microcalipers" in aqueous solutions of polyvinyl alcohol (PVA), we estimated the drag using the Stokes equation,[49-51] $F_{\mathrm{d}} = -3\,\pi\,\eta\,v_{\mathrm{m}}\,d_{\mathrm{V}}\,\chi$, where η is effective viscosity of the fluid, v_{m} (= D / time to fold) is velocity of an arm of the microbot during folding at $\vec{H} = 0$ G, $d_{\mathrm{V}} = (6\,V\,/\,\pi)^{1/3}$ is the diameter of a sphere with the same volume V as the inclusion, and χ is a shape factor. In our estimation, we used $V = 2L^3$ (one arm of the microbot) and $\chi = 1.12$ for a cluster of two spheres ($\chi = 1$ for a sphere). We made aqueous solutions with different concentrations of PVA and measured their viscosities at shear rates between 3 and 30 sec^{-1} (Figure S3, Supporting Information; AR-G2, TA Instruments Ltd.). We then correlated η with the average folding time for the microbots in each PVA solution (Figure 6a). The composition of each PVA solution was confirmed using a pycnometer (inset of Figure 6a). Low concentrations of PVA are considered near-Newtonian,[52] thus we overlaid predictions of their η using the Eyring viscosity model (see Supporting Information for details), and we found that the experimental values agree well with theory.[53] We generated calibration curves of η for microbots energized by

$\vec{H}$ = 70 G (Figure 6b). Then, we determined the average F_d across all viscosities tested and used this as an estimation of the magnetic dipolar force (–34.6 ± 4.0 pN; Figure 6c (right)).

We calculated the overall driving force (Figure 6d) for each condition by adding the residual magnetic dipolar force (–34.6 ± 4.0 pN) to the forces resulting from LC elastic and defect energies ($F_n \approx \Delta E_n / D$); F_1 = –29.2 pN, F_2 = 11.4 pN, F_3 = –14.0 pN, and F_4 = 26.6 pN. These findings, as shown in Figure 6d, are in general agreement with the folding dynamics of the microbot upon removal of $\vec{H}$ (Figure 2c), as the negative values of the overall driving force confirm that the off-state is favored for all conditions. We note, however, that one set of experimental observations did not follow the correlation between folding dynamics and overall driving force. Specifically, we found the folding times of non-treated microbots in planar and homeotropic optical cells (Figure 2c) to be similar, while the overall driving force predicts a faster folding motion of microbots in a planar optical cell ($\Delta E_1 < \Delta E_3$; Figure 6d). This discrepancy suggests that the folding dynamics of microbots not only depend on the net forces driving their folding motions, but also on orientation-dependent resistances that slow down the folding motion.

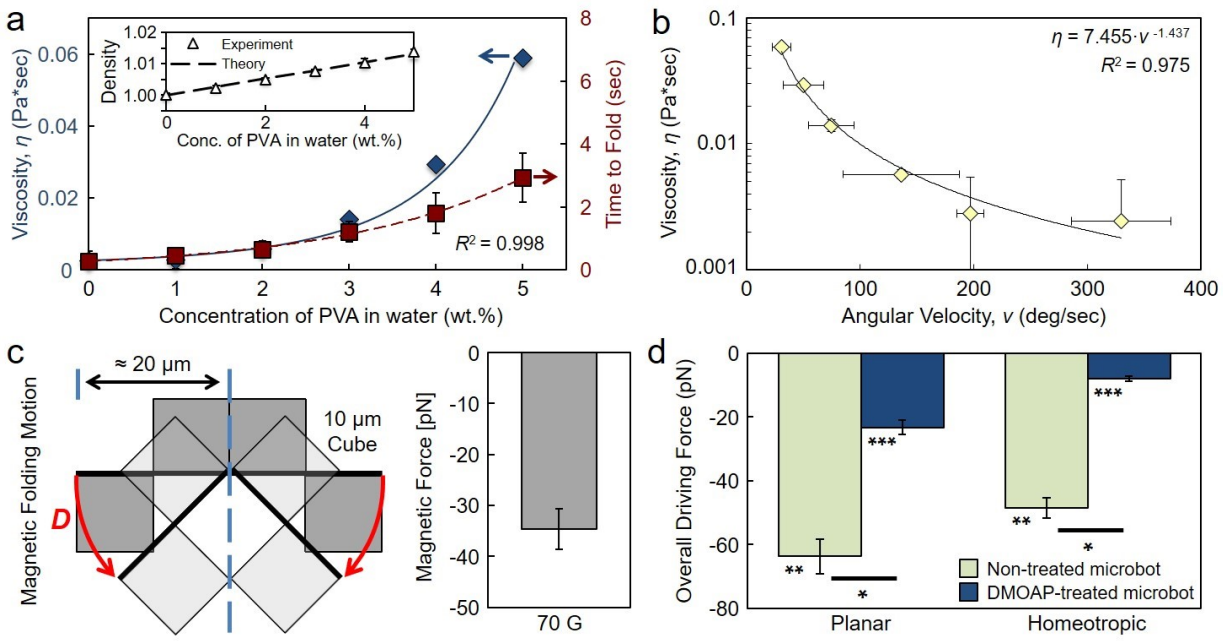

Figure 6. Overall driving force guiding microbot dynamics in LC. a) Average viscosity, η, of various PVA solutions (diamonds, left) and the corresponding time for microbots to fold (squares, right; $\vec{H}$ = 70 → 0 G). Data represent mean ± S.D.; $N \geq 8$. Solid line indicates the two-component Eyring viscosity model. Dashed line reveals an exponential fit of the absolute time for the microbots to fold. Inset indicates the theoretical and empirical density of PVA solutions, confirming their composition. b) Correlation between angular velocity of microbots with measured η. Data represent mean ± S.D.; N = 8. c) [Left] Schematic illustration of a microbot in an extended ($\vec{H}$ = 70 G) and a folded ($\vec{H}$ = 0 G) configuration; [Right] estimated magnetic dipolar force from microbots after removing the field of $\vec{H}$ = 70 G. d) Overall driving force of the microbots, determined by the addition of forces from elastic strain, topological defects, and magnetic dipole. Statistical analyses were performed between groups using Tukey's tests; results marked with asterisks (*, **, or ***) indicate statistical significance between groups with corresponding asterisks ($p < 0.05$). Data represent mean ± S.D.; $N \geq 4$.

We investigated the origins of two possible orientation-dependent resistances: (i) the anisotropic viscosity of nematic 5CB and (ii) frictional interaction with confining surfaces, as influenced by levitation of the microbots in the LC. We consider each in turn. First, LCs exhibit three viscosities (η_1, η_2, and η_3)[54-55] that are defined by the relative directions of **n**, the flow

velocity ($\boldsymbol{v}_f$), and the velocity gradient ($\nabla \boldsymbol{v}_f$); η_1 for $\mathbf{n} \parallel \boldsymbol{v}_f$, η_2 for $\mathbf{n} \parallel \nabla \boldsymbol{v}_f$, and η_3 for $\mathbf{n} \perp \boldsymbol{v}_f$ and $\nabla \boldsymbol{v}_f$. Therefore, the viscous drag experienced by microbots in planar optical cells (Figure 4) will be dominated by η_1 and η_2, whereas microbots in homeotropic optical cells (Figure 5) will experience η_3 as the dominant viscosity. Since η_2 (= 0.098 Ps·s) > η_3 (= 0.035 Ps·s) > η_1 (= 0.020 Ps·s) at 27°C for 5CB,[56] the viscous drag experienced by non-treated microbots in planar optical cells ($(\eta_1 + \eta_2) / 2$ = 0.059 Ps·s) will be greater than that in homeotropic optical cells (η_3 = 0.035 Ps·s).

Second, elastic strain of LC confined between the microbots and bounding surfaces of the optical cell will generate a repulsive force, thus levitating the microbots above the bounding surface to a height determined by a balance between gravitational and the elastic repulsive forces.[22, 57-58] We estimated the levitation height for non-treated microcubes in planar and homeotropic optical cells to be $h_P \sim 0.6$ μm and $h_H \sim 1.1$ μm, respectively (Figure S4, Supporting Information). Accordingly, the actuation of a microbot in a planar optical cell should encounter stronger frictional resistances than that a microbot in homeotropic optical cell.

In summary, from the two analyses presented above, we conclude that the higher effective viscosity and lower levitation height of non-treated microbots in planar optical cells, as compared to homeotropic optical cells, will generate greater overall resistance to motion. This greater motion resistance can potentially lead to similar folding times of non-treated microbots in planar and homeotropic optical cells (Figure 2c) in the presence of a greater overall driving force in a planar optical cell (Figure 6d).

3. Conclusions

In this study, we found that LCs can be used to strongly influence the folding dynamics of reconfigurable microbots. The effect of the LC can be tuned by the surface anchoring of LC on the microbots and the far-field orientation of LCs by the walls of the experimental chambers. These factors determine the local structuring of LC and the formation of LC topological defects around the microbots, giving rise to two groups of effects controlling the dynamics of microbot reconfiguration: changes in viscous drag and differences in the LC elastic and defect free energy. Whereas the LC elastic energy can facilitate or oppose folding of the microbots (depending on surface anchoring of the LC), we found that the folded states of the microbots generate additional LC defects whose energetic effect is to resist transition to folded states. Thus, by understanding LC-related factors that influence the driving force and resistance for folding, and by applying them as a set of general design rules, it is possible to attain control of the dynamics of reconfigurable microscale structures in ways that are not possible in isotropic liquid environments.

The change in the dynamics of the assemblies allows to gain physical insight on the role of the energy of LC anchoring on the microbot-medium interactions. For example, we measure substantially slower rate of actuation by modifying the surfaces of the microcube assembly blocks to have perpendicular instead of planar LC anchoring (as done by surface modifications with DMOAP). One interesting possibility for future investigation is whether decreasing the magnetic moment by using lower field strengths, smaller particles, or thinner ferromagnetic patches could reduce the magnetic driving force and allow DMOAP-treated microbots to remain open in nematic phases, but not in isotropic phases. Alternatively, by orienting the long axis of an actuator parallel to $\mathbf{n}_0$ (as opposed to orthogonal, as shown in the case of the homeotropic optical cell), it is possible to use the elastic forces in the LCs increase the speed of folding actuation.

Our results also suggest multiple insights relayed to the design of microbots operating in complex medium. By selectively modifying the microcube surfaces, it should be possible, for example, to locally control their mutual orientation and achieve assembly of specific microbot sequences with controlled folding dynamics. The microbots can serve as calipers that test the microrheological properties of their media, or that detect microscale structural changes in their environment. On the other hand, the ability of LCs to change orientation in response to weak cues (e.g., chemical additives, electric fields, and temperature) could also enable additional means of programming the dynamics of reconfigurable microdevices and mechanically actuated microswimmers.[22] We believe that the general principles reported in our paper can be extended to other types of LC media, including biocompatible LCs such as lyotropic chromonic LC[59-61] or dense anisotropic biologically-derived fluids.[62-63]

4. Experimental Section

Materials. Nematic liquid crystal was purchased from HCCH (5CB; Jiangsu Hecheng Display Technology Co., Ltd). Single-side polished silicon wafers were purchased from Addison Engineering, Inc.. Negative photoresist used as the base material for the microcubes (SU-8 10) was purchased from MicroChem, Co. Dimethyloctadecyl[3-(trimethoxysilyl)propyl] ammonium chloride (DMOAP) was purchased form Millipore Sigma, Co. The polymeric alignment layers were purchased from HD Microsystems, LLC and Nissan Chemical, Ltd., respectively (PI2555 and SE5661). Transmission electron microscopy (TEM) grids with 20 μm in thickness were purchased from Electron Microscopy Sciences, Inc. Double-sided tape was used directly from the manufacturer (3M, Co.).

Preparation of microcubes. Microcubes with an edge length of 10 μm were fabricated on single-side polished silicon wafers using SU-8 via photolithography following procedures

described previously.[20, 64-65] A magnetic film on one side of microcubes was obtained by depositing films of Chromium (10 nm in thickness) followed by Cobalt (100 nm in thickness) via metal evaporation. Patchy microcubes were extracted from the wafers using a rubber policeman. Microcubes treated with DMOAP were treated prior to their magnetic assembly. Dry microcubes were added to a 1.0 vol.% aqueous solution of DMOAP and the solution was sonicated for 10 min. Next, the solution was centrifuged at 8,000 × g for 2 min, the supernatant was aspirated, and the pellet of microcubes was dried in a vacuum oven (ADP21; Yamato Scientific America, Inc.) at 90°C for 30 min. Finally, the microcubes were mixed in their carrier solution (i.e., water, aqueous PVA mixtures (145 kDa), or 5CB).

Preparation of optical cells. Optical cells were assembled from flat glass plates coated with polyimide films of PI2555 for planar optical cells (the far-field director $\mathbf{n}_0$ is parallel to bounding plates) or SE5661 for homeotropic optical cells ($\mathbf{n}_0$ is perpendicular to bounding plates). PI2555 substrates were rubbed 10 times with velvet to achieve unidirectional alignment of $\mathbf{n}_0$ and were assembled in an anti-parallel fashion. The gaps (100–300 μm) between the plates were set by using double-sided tape of well-defined thickness.

Magnetic field assembly and actuation. The magnetic assembly setup comprised a collinear pair of electromagnetic coils powered by a DC power supply (382260; Extech Instruments Co.). The gap between the coils was fixed to 4 cm where an assembly chamber was placed on the center, and the field strength was measured using a gaussmeter (GM2; AlphaLab Inc.). We note that fields the highest magnetic field strengths used (i.e., $\vec{H}$ = 70 G) were insufficient to reorient the LC molecules by the field alone.[66]

Supporting Information

Supporting Information is available from the Wiley Online Library or from the author.

Acknowledgements

This work was supported by the National Science Foundation's (NSF's) Research Triangle Materials Research Science and Engineering Center (MRSEC, DMR-1121107), the Army Research Office (W911NF-19-1-0071), and the National Science Foundation (CBET-1803409 and CBET-1604116). Analyses of the topological defects were performed with support from Department of Energy, Basic Energy Sciences, Division of Materials Research, Biomaterials Program under Grant No. DE-SC0004025. Microcubes were fabricated in the Shared Materials Instrumentation Facility at Duke University, which is a member of the North Carolina Research Triangle Nanotechnology Network and is supported by the NSF (ECCS-1542015) as part of the National Nanotechnology Coordinated Infrastructure.

Conflicts of Interest

The authors declare no conflict of interest.

References

[1] C. L. Randall, E. Gultepe, D. H. Gracias, *Trends Biotechnol* **2012**, *30*, 138.

[2] J. Yan, M. Han, J. Zhang, C. Xu, E. Luijten, S. Granick, *Nat. Mater.* **2016**, *15*, 1095.

[3] K. Han, C. W. Shields, O. D. Velev, *Adv. Funct. Mater.* **2018**, *28*, 1705953.

[4] S. Tasoglu, E. Diller, S. Guven, M. Sitti, U. Demirci, *Nat Commun* **2014**, *5*, 3124.

[5] M. Z. Miskin, K. J. Dorsey, B. Bircan, Y. Han, D. A. Muller, P. L. McEuen, I. Cohen, *PNAS* **2018**, *115*, 466.

[6] B. Bharti, A. L. Fameau, M. Rubinstein, O. D. Velev, *Nat. Mater.* **2015**, *14*, 1104.

[7] M. Nakahata, Y. Takashima, H. Yamaguchi, A. Harada, *Nat Commun* **2011**, *2*, 511.

[8] J. Y. Ou, E. Plum, L. Jiang, N. I. Zheludev, *Nano Lett* **2011**, *11*, 2142.

[9] Q. Wang, E. T. F. Rogers, B. Gholipour, C. M. Wang, G. H. Yuan, J. H. Teng, N. I. Zheludev, *Nat. Photonics* **2016**, *10*, 60.

[10] S. K. Smoukov, S. Gangwal, M. Marquez, O. D. Velev, *Soft Matter* **2009**, *5*, 1285.

[11] T. Qiu, T. C. Lee, A. G. Mark, K. I. Morozov, R. Munster, O. Mierka, S. Turek, A. M. Leshansky, P. Fischer, *Nat Commun* **2014**, *5*, 5119.

[12] G. Kokot, D. Piet, G. M. Whitesides, I. S. Aranson, A. Snezhko, *Sci. Rep.* **2015**, *5*, 9528.

[13] A. A. Shah, B. Schultz, W. J. Zhang, S. C. Glotzer, M. J. Solomon, *Nat. Mater.* **2015**, *14*, 117.

[14] U. Ohiri, C. W. Shields, K. Han, T. Tyler, O. D. Velev, N. Jokerst, *Nat Commun* **2018**, *9*, 1791.

[15] C. W. Shields, K. Han, F. D. Ma, T. Miloh, G. Yossifon, O. D. Velev, *Adv. Funct. Mater.* **2018**, *28*, 1803465.

[16] Y. Yuan, G. N. Abuhaimed, Q. K. Liu, I. I. Smalyukh, *Nat Commun* **2018**, *9*, 5040.

[17] S. Spagnolie, *Complex Fluids in Biological Systems*, Springer-Verlag New York, New York **2015**.

[18] P. G. de Gennes, J. Prost, *The Physics of Liquid Crystals*, Clarendon Press, Oxford **1993**.

[19] D. Demus, J. Goodby, G. W. Gray, H.-W. Spiess, V. Vill, *Handbook of Liquid Crystals*, Wiley-VCH Verlag GmbH, New York **1998**.

[20] K. Han, C. W. Shields, N. M. Diwakar, B. Bharti, G. P. Lopez, O. D. Velev, *Sci. Adv.* **2017**, *3*, e1701108.

[21] T. A. Wood, J. S. Lintuvuori, A. B. Schofield, D. Marenduzzo, W. C. K. Poon, *Science* **2011**, *334*, 79.

[22] Y.-K. Kim, X. Wang, P. Mondkar, E. Bukusoglu, N. L. Abbott, *Nature* **2018**, *557*, 539.

[23] K. C. K. Cheng, M. A. Bedolla-Pantoja, Y.-K. Kim, J. V. Gregory, F. Xie, A. de France, C. Hussal, K. Sun, N. L. Abbott, J. Lahann, *Science* **2018**, *362*, 804.

[24] Y.-K. Kim, S. V. Shiyanovskii, O. D. Lavrentovich, *J. Phys.-Condes. Matter* **2013**, *25*, 404202.

[25] M. Kleman, O. D. Lavrentovich, *Soft Matter Physics: An Introduction*, Springer, New York **2003**.

[26] X. Wang, Y. Zhou, Y.-K. Kim, D. S. Miller, R. Zhang, J. A. Martinez-Gonzalez, E. Bukusoglu, B. Zhang, T. M. Brown, J. J. de Pablo, N. L. Abbott, *Soft Matter* **2017**, *13*, 5714.

[27] B. Senyuk, Q. K. Liu, Y. Yuan, I. I. Smalyukh, *Phys Rev E* **2016**, *93*, 062704.

[28] Y.-K. Kim, G. Cukrov, F. Vita, E. Scharrer, E. T. Samulski, O. Francescangeli, O. D. Lavrentovich, *Phys Rev E* **2016**, *93*, 062701.

[29] Y.-K. Kim, B. Senyuk, S. T. Shin, A. Kohlmeier, G. H. Mehl, O. D. Lavrentovich, *Soft Matter* **2014**, *10*, 500.

[30] B. Senyuk, Q. K. Liu, S. L. He, R. D. Kamien, R. B. Kusner, T. C. Lubensky, I. I. Smalyukh, *Nature* **2013**, *493*, 200.

[31] Q. K. Liu, B. Senyuk, M. Tasinkevych, I. I. Smalyukh, *PNAS* **2013**, *110*, 9231.

[32] P. M. Phillips, A. D. Rey, *Soft Matter* **2011**, *7*, 2052.

[33] D. A. Beller, M. A. Gharbi, I. B. Liu, *Soft Matter* **2015**, *11*, 1078.

[34] M. V. Rasna, K. P. Zuhail, U. V. Ramudu, R. Chandrasekar, J. Dontabhaktuni, S. Dhara, *Soft Matter* **2015**, *11*, 7674.

[35] I. I. Smalyukh, *Annu Rev Conden Ma P* **2018**, *9*, 207.

[36] J. Dontabhaktuni, M. Ravnik, S. Zumer, *Soft Matter* **2012**, *8*, 1657.

[37] U. Tkalec, M. Skarabot, I. Musevic, *Soft Matter* **2008**, *4*, 2402.

[38] B. Senyuk, M. B. Pandey, Q. K. Liu, M. Tasinkevych, I. I. Smalyukh, *Soft Matter* **2015**, *11*, 8758.

[39] B. X. Li, V. Borshch, R. L. Xiao, S. Paladugu, T. Turiv, S. V. Shiyanovskii, O. D. Lavrentovich, *Nat Commun* **2018**, *9*, 2912.

[40] Y. D. Gu, N. L. Abbott, *Phys. Rev. Lett.* **2000**, *85*, 4719.

[41] I. Lazo, C. H. Peng, J. Xiang, S. V. Shiyanovskii, O. D. Lavrentovich, *Nat Commun* **2014**, *5*, 5033.

[42] Y. M. Luo, D. A. Beller, G. Boniello, F. Serra, K. J. Stebe, *Nat Commun* **2018**, *9*, 3841.

[43] M. Cavallaro, M. A. Gharbi, D. A. Beller, S. Copar, Z. Shi, T. Baumgart, S. Yang, R. D. Kamien, K. J. Stebe, *PNAS* **2013**, *110*, 18804.

[44] Y.-K. Kim, K. R. Raghupathi, J. S. Pendery, P. Khomein, U. Sridhar, J. J. Pablo, S. Thayumanavan, N. L. Abbott, *Langmuir* **2018**, *34*, 10092.

[45] X. G. Wang, Y.-K. Kim, E. Bukusoglu, B. Zhang, D. S. Miller, N. L. Abbott, *Phys. Rev. Lett.* **2016**, *116*, 147801.

[46] H. Stark, *Phys. Rep.* **2001**, *351*, 387.

[47] T. C. Lubensky, D. Pettey, N. Currier, H. Stark, *Phys Rev E* **1998**, *57*, 610.

[48] L. Pleskacz, E. Fornalik-Wajs, *J. Phys. Conf. Ser.* **2014**, *530*, 012062.

[49] J. C. Loudet, P. Hanusse, P. Poulin, *Science* **2004**, *306*, 1525.

[50] D. Leith, *Aerosol Sci Tech* **1987**, *6*, 153.

[51] Y. S. Cheng, *Chem. Eng. Commun.* **1991**, *108*, 201.

[52] H. W. Gao, J. Y. He, R. J. Yang, L. Yang, *J. Appl. Polym. Sci.* **2010**, *116*, 2734.

[53] V. A. Bloomfield, R. K. Dewan, *J. Phys. Chem.* **1971**, *75*, 3113.

[54] M. Miesowicz, *Nature* **1946**, *158*, 27.

[55] A. Sengupta, S. Herminghaus, C. Bahr, *Liq. Cryst. Rev.* **2014**, *2*, 73.

[56] A. G. Chmielewski, *Mol. Cryst. Liq. Cryst.* **1986**, *132*, 339.

[57] O. P. Pishnyak, S. Tang, J. R. Kelly, S. V. Shiyanovskii, O. D. Lavrentovich, *Phys. Rev. Lett.* **2007**, *99*, 127802.

[58] S. B. Chernyshuk, B. I. Lev, *Phys Rev E* **2011**, *84*, 011707.

[59] L. L. Cheng, Y. Y. Luk, C. J. Murphy, B. A. Israel, N. L. Abbott, *Biomaterials* **2005**, *26*, 7173.

[60] J. Lydon, *J. Mater. Chem.* **2010**, *20*, 10071.

[61] R. R. Trivedi, R. Maeda, N. L. Abbott, S. E. Spagnolie, D. B. Weibel, *Soft Matter* **2015**, *11*, 8404.

[62] S. Zhou, A. Sokolov, O. D. Lavrentovich, I. S. Aranson, *PNAS* **2014**, *111*, 1265.

[63] G. Ariel, M. Sidortsov, S. D. Ryan, S. Heidenreich, M. Bar, A. Be'er, *Phys Rev E* **2018**, *98*, 032415.

[64] C. W. Shields, S. Zhu, Y. Yang, B. Bharti, J. Liu, B. B. Yellen, O. D. Velev, G. P. Lopez, *Soft Matter* **2013**, *9*, 9219.

[65] P. Y. Wang, C. W. Shields, T. H. Zhao, H. Jami, G. P. Lopez, P. Kingshott, *Small* **2016**, *12*, 1309.

[66] M. I. Boamfa, S. V. Lazarenko, E. C. M. Vermolen, A. Kirilyuk, T. Rasing, *Adv. Mater.* **2005**, *17*, 610.